Journal of Materials Chemistry A

ROYAL SOCIETY OF CHEMISTRY

PAPER

View Article Online
View Journal | View Issue

Cite this: J. Mater. Chem. A, 2023, 11, 24261

Two-dimensional nickel cyano-bridged coordination polymer thermally derived potent electrocatalysts for alkaline hydrogen evolution reaction†

Manar M. Abdel Naby, [ab] Mohamed B. Zakaria, *[cd] Haitham M. El-Bery, [e] Gehad G. Mohamed[af] and Mohamed E. El-Khouly *[a]

Received 29th July 2023
Accepted 13th October 2023

DOI: 10.1039/d3ta04511k

rsc.li/materials-a

Because of its sustainability and cleanliness, hydrogen has recently been a research focus as a potential fuel. One promising way to produce hydrogen is water electrolysis in an alkaline solution. However, this process requires much energy to split the H–OH bond and transfer multiple electrons/protons. To overcome this challenge, catalytic electrodes have been developed to reduce the energy needed and maintain sustainable water electrolysis. This study explores the potential of utilizing a two-dimensional nickel-based cyanide coordination polymer (2D Ni-CP) precursor to synthesize effective Ni-based inorganic nanostructured electrodes. Various types of electrodes, including Ni-O, Ni-S, Ni-Se, and Ni-P, are synthesized through direct thermal treatment of the coordination polymer. The performance of the as-prepared materials in the hydrogen evolution process (HER) in an alkaline medium is examined. Ni-P demonstrates the most promising HER performance with an overpotential of 266 mV at 10 mA cm^{-2} and a Tafel slope of 186 mV dec^{-1}. These results are compared to those of the benchmark expensive and scarce Pt/C-40% catalyst (38 mV and 48 mV dec^{-1}) examined under identical conditions. Additionally, Ni-P shows outstanding HER durability over four days, as reflected by chronopotentiometry measurements.

1. Introduction

Developing novel renewable energy resources that reduce global warming and compensate for the depletion of energy sources is of great interest nowadays.[1–4] Numerous energy conversion devices, including solar cells, electrolyzers, and fuel cells, are research subjects because they are environmentally friendly technologies with readily available inputs.[5,6] Although there is a large body of research on many types of solar cells, the highest efficiency for terrestrial conditions up to 2022 is 39.5%.[7] The quantity of sun hours, related to weather and geological location, is another factor that determines how much electricity a solar system can generate.[8] On the other hand, employing water electrolyzers has emerged recently as a competitive way to using solar cells for green hydrogen production with zero carbon emissions. Hydrogen-feeding fuel cells produce clean electricity eligible for houses, factories, and electric vehicles.

So far, water has been proposed as a hydrogen source through the overall electrochemical water splitting. The oxygen evolution reaction (OER) and the hydrogen evolution reaction (HER) are the two half-cell reactions. The HER is a lethargic reaction, particularly in alkaline media, because they mainly contain OH^- groups and water molecules, so the creation of active H* is difficult. The step of H* formation through the H_2O dissociation stage is known as the Volmer step, which requires the breakage of the HO–H covalent bond. Finally, another H* is created to form an H_2 molecule. The HO–H bond breakage step demands high energy (*e.g.*, overpotential), which requires powerful industrially applicable catalysts.[9–11]

The scarce (Pt)-based nanostructured materials are the strongest benchmark HER catalysts, but their limited availability and high cost prevent widespread use. Consequently, the current research efforts strive to develop efficient HER electrocatalysts based on earth-abundant elements.[12,13] Transition metal-based oxides, sulfides, selenides, phosphides, nitrides, and carbides have attracted research attention due to their high

[a]Institute of Basic and Applied Science, Egypt-Japan University of Science and Technology (E-JUST), New Borg El-Arab City, Alexandria, Egypt. E-mail: mohamed.elkhouly@ejust.edu.eg

[b]Department of Chemistry, Faculty of Science, Ain Shams University, Cairo, Egypt

[c]Department of Chemistry, Faculty of Science, Tanta University, 31527, Tanta, Egypt. E-mail: mohamed.hegazy3@science.tanta.edu.eg

[d]Alexander von Humboldt (AvH) Foundation, 53173, Bonn, Germany

[e]Department of Chemistry, Green Hydrogen Production Laboratory, Faculty of Science, Assiut University, Assiut, 71515, Egypt

[f]Department of Chemistry, Faculty of Science, Cairo University, Cairo, Egypt

† Electronic supplementary information (ESI) available. See DOI: https://doi.org/10.1039/d3ta04511k

catalytic activity for electrochemical water splitting in general.[14–23] Nickel oxides (NiO), chalcogenides (Ni_xS_y and Ni_xSe_y), and phosphides (Ni_xP_y) are particularly noteworthy among these compounds due to their exceptional inherent redox characteristics, durability, and resistance to the reduction process, as well as their abundance in the earth's crust. As a result, they have recently gained significant attention from researchers.[1,9,24–33]

Along with composition regulation, the final shape is essential for the catalytic characteristics. Accessible pores also significantly increase the number of active sites per particle, which benefits the charge-transfer process. The mainstream usually has used the solvothermal technique to produce metal-based electrocatalysts. Many self-supported electrodes with catalysts of sheet or array morphologies have recently been prepared. Wang *et al.* have designed a NiO array on Ni foam (NF) with an overpotential of −163 mV at 10 mA cm^{-2}, while Faid *et al.* have reported NiO nanosheets drop-cast on glassy carbon, which gave an overpotential of −372 mV at the same current density.[34,35] However, some drawbacks hinder generalizing the solvothermal pathway. First, using the solvothermal technique in catalyst preparation is sophisticated and more suitable for bench-scale preparation, whereas it needs advanced high-priced autoclaves to work under complex conditions of controlling temperature and pressure during crystal formation. Also, the preparation process cannot be observed, so problems cannot be detected earlier.[36] As a result, the gap in this area still needs modification to get a more accessible synthesis pathway of efficient nanostructured catalysts for the HER.

This paper describes a versatile method for fabricating nanostructured nickel-based oxide, sulfide, selenide, and phosphide, starting with rationally designed 2D Ni-CP flakes. This starting polymer displays a nano-porous structure of layered nanosheets. Ni-based oxide, sulfide, selenide, and phosphide are successfully produced after annealing in the presence of the heteroatom source. Notably, the morphology of the polymer helps get uniform particles with morphology in the nano-regime after the annealing process to achieve surface active sites as much as possible. This synthesis process has several pros compared with the most common preparation methodology. First, it helps to synthesize diverse Ni compounds by aiding one precursor through a one-step process because of the –CN group elimination simplicity. Also, it has product phase flexibility through adapting the ratio and temperature. Second, there is no high sensitivity toward pressure control or the nature of the added compounds or concentrations. Additionally, it is a fast synthesis method, a cost-effective process with readily available compounds and simple equipment.[37,38]

Hence, by applying the simple drop-casting electrode preparation method, all nickel compounds show catalytic activity towards the HER, especially Ni-P and Ni-S. Catalytic activity tests are performed in potassium hydroxide solution (KOH; 0.1 M) and the results are comparable to those of scarce and expensive Pt/C-40% electrocatalysts. Furthermore, all the synthesized electrocatalysts display superior durability in chronopotentiometry for 24 hours compared to Pt/C-40%. In contrast, Ni-based phosphide shows potent behavior during four days of catalytic HER performance tests.

2. Experimental section

2.1. Chemicals and reagents

Potassium cyanide (KCN), nickel(II) chloride hexahydrate ($NiCl_2 \cdot 6H_2O$), thiourea (NH_2CSNH_2), and trisodium citrate dihydrate (TSCD, $C_6H_9Na_3O_9$) were purchased from Sigma Aldrich. Ethanol (EtOH), potassium hydroxide (KOH), ammonia solution ($NH_3 \cdot H_2O$), and triphenylphosphine (Ph_3P) were purchased from Fisher Scientific. Both the selenium powder (Se, 99%) and the Nafion D-520 dispersion (5% w/w in water and *n*-propanol) were bought from Alfa Aesar. Without any additional purification, each reagent was used as received.

2.1.1 Synthesis of the potassium tetracyanonickelate(II) complex. To synthesize the $K_2[Ni(CN)_4] \cdot xH_2O$ complex, 5.10 g of nickel chloride and 3.20 g of potassium cyanide were dissolved in 20 and 7 mL of deionized water (DW), respectively. KCN solution was added to the Ni(II) solution dropwise with continuous stirring to get the grayish-green precipitate of nickel cyanide. The precipitate was filtered, washed with DW, and dissolved in another colorless KCN solution (3.35 g/15 mL). The red solution obtained was heated at 100 °C until the excess water evaporated. Subsequently, the remaining solution was allowed to form reddish-orange complex crystals at room temperature. The resultant crystals were dried at 100 °C for an hour to produce a pale-yellow crystalline powder of potassium tetracyanonickelate(II) complex, which was then used for further processing.[39]

2.1.2 Synthesis of 2D Ni-CP flakes. 1.45 g of $K_2[Ni(CN)_4] \cdot xH_2O$ complex was dissolved in 150 mL of DW, and then the solution was added dropwise to 150 mL of a mixed solution of $NiCl_2 \cdot 6H_2O$ (1.42 g) and TSCD (1.32 g) under constant magnetic stirring. The mixture was left on a stirrer plate for 1 hour until a green Ni-CP precipitate was formed. After that, the vial was transferred to a fume hood for aging for one day. The precipitate was centrifuged several times with DW and ethanol to wash it, and it was then allowed to dry at room temperature.[9]

2.1.3 Synthesis of NiO from 2D Ni-CP (Ni-O). To transform 2D Ni-CP into black NiO nanoparticles, a quantity of 500 mg of the coordination polymer was subjected to annealing in a ceramic crucible under aerobic conditions. This procedure was run for 4 hours at a temperature of 300 °C and a heating rate of 1.0 °C per minute.[38]

2.1.4 Synthesis of the amorphous NiO reference (r-NiO). A usual co-precipitation process was used to prepare amorphous r-NiO for electrochemical behavior comparison. A nickel chloride solution was initially obtained by dissolving 10.19 g in 107 mL of DW. Then, diluted ammonia solution (50%) was added to the former solution dropwise under stirring to get the $Ni(OH)_2$ precipitate. Simultaneously, a pH meter monitored the solution pH until it reached 9 to terminate the reaction. The beaker containing the nickel hydroxide precipitate was put into a water bath at 70 °C for 2 hours until the remaining Ni ions interacted, and excess ammonia evaporated. The final step involved washing the pale green precipitate with DW/EtOH and annealing at 400 °C under aerobic conditions. The heating rate

was 4 °C per hour, and the process was carried out for 1 hour, producing deep gray r-NiO nanoparticles.[40]

2.1.5 Synthesis of Ni-sulfide (Ni-S), Ni-selenide (Ni-Se), and Ni-phosphide (Ni-P) nanoparticles from 2D Ni-CP. The three electrocatalysts were prepared by annealing of 2D Ni-CP flakes in a porcelain-boat, inside a tubular furnace operated under an Ar atmosphere in the presence of the anion source with respect to each material. To begin the synthesis of Ni-S, 175 mg of Ni-CP was mixed gently with 700 mg of thiourea (at a ratio of 1/4 wt/wt%). The resulting mixture was annealed at 450 °C for one hour, with a heating rate of 5 °C per minute. This process yielded a composite material consisting of NiS and NiS_2.[9] Similarly, Ni-Se was produced by gently grinding 300 mg of 2D Ni-CP with 600 mg of Se powder. The resulting mixture was then annealed at 400 °C for 3 hours, with a heating rate of 2 °C per minute.[41] Finally, 2D Ni-CP (500 mg) was ground smoothly with triphenylphosphine (500 mg) to get Ni-P after annealing. The annealing process was carried out in two stages. First, the mixture was heated to 300 °C at a rate of 2.5 °C per minute and held at that temperature for 2 hours. Subsequently, the temperature was increased to 750 °C at a rate of 2.5 °C per minute and maintained at that temperature for 4 hours. Following this, the mixture was allowed to cool naturally, and the resulting Ni-P powder was collected for characterization and electrochemical measurements.[26]

2.2. Characterization

A field emission scanning electron microscope (FESEM, Thermo Fisher Scientific Quattro S) was used to collect the images of the morphological structure. Powder X-ray diffraction patterns were detected on an X-ray diffraction instrument (PXRD, Bruker D8 Discover X-ray Diffractometer). The oxidation states and elemental compositions of the samples were investigated by X-ray photoelectron spectroscopy (XPS, Thermo Fisher Scientific K-Alpha XPS). The absorption spectra were recorded using UV-Visible spectrophotometer (Shimadzu, model 2600).

2.3. Electrochemical measurements

The electrochemical HER measurements were done on a CS350 single-channel potentiostat/galvanostat instrument equipped with a three-electrode flow cell. The reference electrode (RE) used was a mercury-mercuric oxide with 1.0 M KOH solution, and the working electrode (WE) was a carbon paper with an area of 0.25 cm^2 (0.5 cm × 0.5 cm) coated with the catalyst. A graphite rod was utilized as the counter electrode (CE), and all measurements were performed in an electrolyte solution of 1.0 M KOH. 950 μL of DW/EtOH solution (3 : 1|v/v) and 5 mg of the catalyst were combined to prepare the catalyst ink, which was then sonicated for 1 hour. Then, 50 μL of Nafion was added to the mixture and remained under sonication for another hour.[42] Later, 10 μL of the ink was drop-cast on an area of 0.25 cm^2 of WE. Linear sweep voltammetry (LSV) was performed in a potential range from 0 V to −1 V *vs.* RHE with a scan rate of 10 mV s^{-1} for the initial assessment of the catalyst. The potential was corrected *versus* RHE according to $E_{RHE} = E_{Hg/HgO} + 0.140 + 0.059pH$. Electrochemical impedance spectroscopy (EIS) was then conducted to calculate the charge transfer speed. At different scan rates, the cyclic voltammetry (CV) test was also performed to evaluate the electrochemical active surface area (ECSA). Then, it was computed by the following equation ECSA $= R_f S$, where R_f is the roughness factor, and S is the used geometric area of carbon paper. R_f was calculated from C_{dl}/C_S where C_{dl} is the capacitance of the electrical double layer, and C_S is the general specific capacitance (30 μF cm^{-2} was the value used in the calculations of this work).[43] dl is considered as the slope of $i = C_{dl}\nu$ where ν is the scan rate, and i is the double layer charging current. C_{dl} was calculated by applying various scan rates (10, 20, 40, 80, 100, and 150 mV s^{-1}) and measuring the corresponding charging current (the vertical width of the CV rectangle at the middle point of the potential window).[9,43] Also, chronopotentiometry (CP) was performed for extended intervals to estimate the long-term stability of the catalysts. Finally, the 3-electrode system was inserted in a 50 mL sealed cell adapted with inlet and outlet gas ports and directly connected to a gas chromatography instrument (GC-2014, Shimadzu, TCD detector, 2 m 80/10 Shincarbon ST packed column and Ar gas as a carrier). The generated H_2 gas was analyzed at 15 minute intervals over 5 hours during the chronopotentiometry test.

3. Results and discussion

The first schematic diagram (Fig. 1) briefly described the synthesis processes of Ni-based materials. First of all, the $K_2[Ni(CN)_4]\cdot xH_2O$ complex was prepared as shown in the experimental part, and its formation was confirmed by measuring the absorption spectrum using a UV-vis spectrometer, where the UV-vis spectrum characteristic of $K_2[Ni(CN)_4]\cdot xH_2O$ was obtained (Fig. S1†).[44] A solution of nickel chloride was mixed slowly with TSCD to form a complex of Ni-citrate. Then, a solution of $K_2[Ni(CN)_4]\cdot xH_2O$ was mixed gently with the Ni–citrate complex. Consequently, a gradual interaction between Ni and $[Ni(CN)_4]^{2-}$ ions leads to the rational formation of 2D Ni-CP flakes. This slow interaction causes the creation of tiny, ordered Hoffman-type sheets of 2D Ni-CP flakes, which are denoted as $Ni(H_2O)_2[Ni(CN)_4]\cdot xH_2O$ in the literature.[38]

SEM pictured all the synthesized materials to confirm their structures and correlate their morphologies with the 2D Ni-CP precursor (Fig. 2a). Annealing of the polymer was done under an oxygenated atmosphere to produce the nickel oxide catalyst with nanoparticle morphology (Fig. 2b), while in an inert atmosphere, the Ni-CP was annealed to produce nickel sulfide, nickel selenide, and nickel phosphide catalysts (Fig. 2c–e). It was evident that the 2D morphology collapsed, resulting in uniform nanoparticles in the nano-regime of Ni-based inorganic materials (Fig. 2b–e). In contrast, the traditional co-precipitation method is used to prepare non-uniform and deformed r-NiO particles (Fig. 2f).[40] The obtained morphology using the 2D Ni-CP precursor revealed its advantage over the traditional precipitation method to form uniform Ni-based inorganic material nanoparticles.

PXRD analysis was used to examine the crystallographic structures and phase purity of the synthesized compounds. The

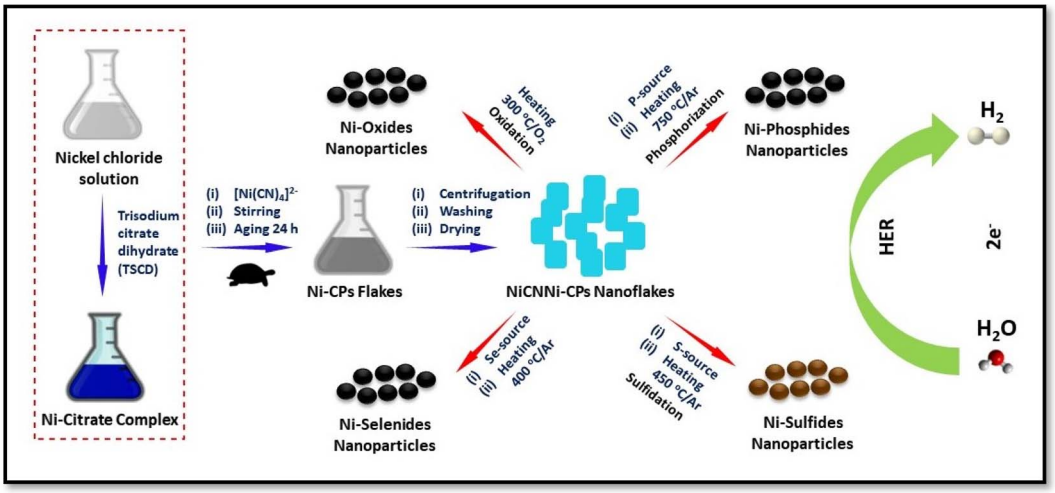

Fig. 1 Schematic illustration of the synthesis process of Ni-based materials.

peaks observed in the XRD pattern of the 2D Ni-CP flakes matched with the orthorhombic Hofmann-type structure of $Ni(H_2O)_2[Ni(CN)_4]\cdot xH_2O$, which possesses a 2D layered structure. This result was consistent with previous literature (Fig. 3a).[38] By annealing 2D Ni-CP at 300 °C under aerobic conditions, a cubic NiO phase was formed (PDF card no. 00-004-0835) (Fig. 3b).[38] Similarly, the annealing of $Ni(OH)_2$ at 400 °C, which was prepared by complexation–precipitation, gave r-NiO structures with a typical XRD pattern (Fig. 3c). The five XRD peaks were assigned with miller indices (111), (200), (220), (311) and (222) characteristic of the cubic NiO phase. Heating the coordination polymer in the presence of thiourea at 450 °C resulted in the appearance of peaks that could be attributed to the NiS and NiS_2 phases (Fig. 3d) with PDF cards of NiS_2 (PDF card no. 65-3325) and hexagonal α-NiS (PDF card no. 02-1280). For nickel selenide (Fig. 3e), the crystal structure was assigned to a pure phase of the cubic structure of $NiSe_2$ (PDF card no. 65-1843), while XRD of the synthesized nickel phosphide (Fig. 3f) revealed the formation of a mixture composed of different Ni-based phosphide phases (*i.e.*, Ni_5P_4, $Ni_{12}P_5$, Ni_2P, and NiP_3) accompanied by predominant metallic Ni atoms with a face-centered cubic shape (PDF card no. 04-0850). Annealing at 750 °C ensured the formation of a Ni-based phosphide phase as well as metallic Ni.[26]

X-ray photoelectron spectroscopy (XPS) confirmed the composition and electronic state of the most efficient catalysts, namely Ni-P, Ni-S, and Ni-Se materials. For Ni-S, the spectrum of Ni showed the two characteristic peaks of Ni $2p_{3/2}$ (855.5 eV) and

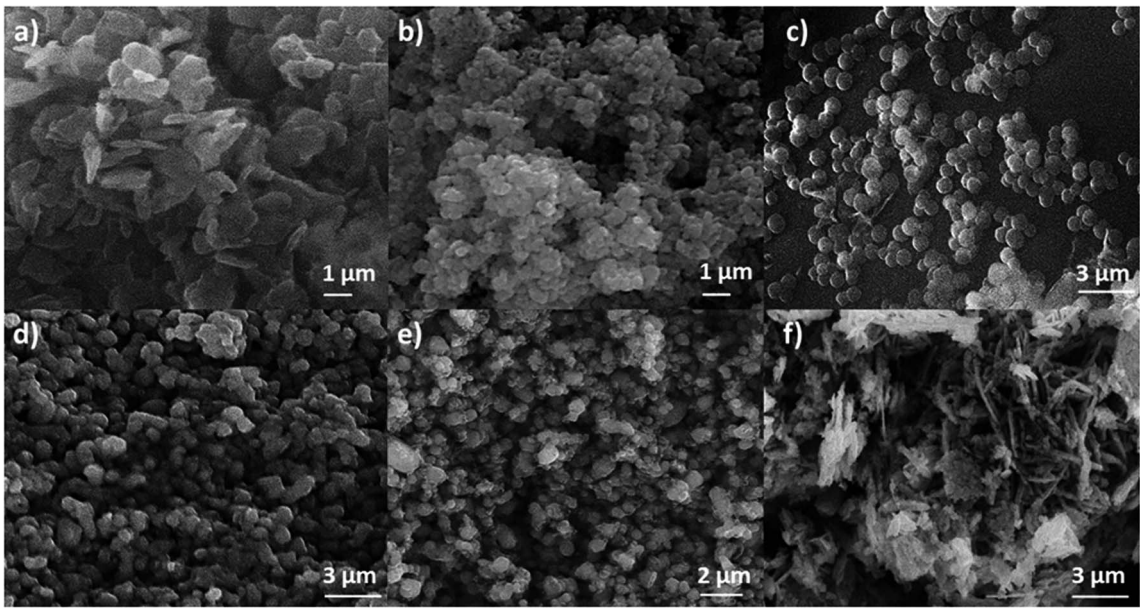

Fig. 2 SEM images of (a) 2D Ni-CP, (b) Ni-O, (c) Ni-S, (d) Ni-Se, (e) Ni-P, and (f) r-NiO.

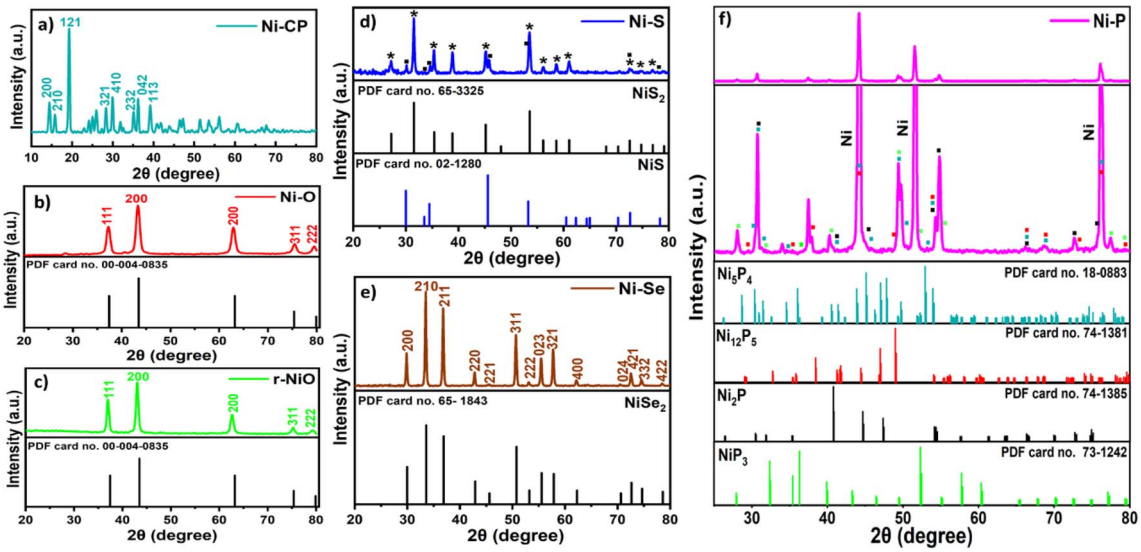

Fig. 3 Powder X-ray diffraction (PXRD) patterns of (a) 2D Ni-CP, (b) Ni-O, (c) r-NiO (d) Ni-S, (e) Ni-Se, and (f) Ni-P.

Ni $2p_{1/2}$ (872.9 eV). These two peaks correspond to $Ni^{\delta+}$; there were four satellite peaks, two peaks for each main characteristic peak, at 861.8, 866.9, 876.5, and 879.3 eV. Also, there were two sub-peaks at 859 and 875.6 eV of oxidized Ni atoms at the Ni-S surface.[45] Notably, Ni-S displayed only two peaks for Ni 2p because the spectra of Ni in NiS and NiS_2 phases were

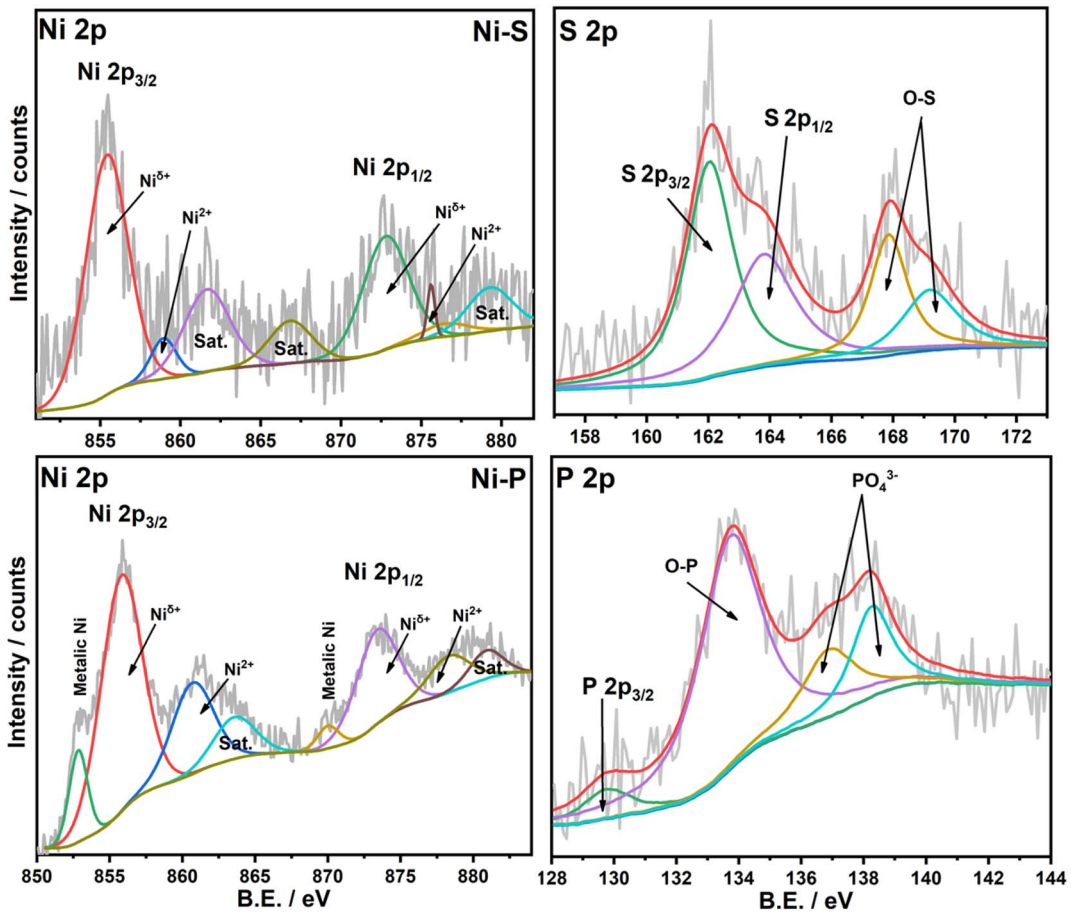

Fig. 4 XPS spectra of the core levels of Ni 2p in Ni-S and Ni-P, S 2p, and P 2p.

convoluted. In addition, two characteristic peaks were detected at 162.1 (S $2p_{1/2}$), and 163.8 eV (S $2p_{1/2}$), which confirmed the presence of a nickel sulfur bond. Additionally, there were two peaks at 167.9 and 169.2 eV of O–S due to Ni-S surface oxidation (Fig. 4).[46,54] For Ni-P, Ni showed four peaks for the Ni $2p_{3/2}$ energy level, which were 852.8 eV (metallic Ni), 855.9 ($Ni^{\delta+}$), 860.8 (oxidized Ni), and 863.7 eV (the satellite peak). Also, there were four peaks for the Ni $2p_{1/2}$ energy level, which were 870 (metallic Ni), 873.6 ($Ni^{\delta+}$), 878.5 (oxidized Ni), and 881.1 eV (the satellite peak). Furthermore, the spectrum of the P peak at 129.7 eV proved the presence of the P $2p_{3/2}$ energy level. The other three peaks (133.8, 137.0, and 138.3 eV) indicated the presence of oxidized phosphorous forms due to Ni-P surface passivation (Fig. 4).[47–49] Eventually, for Ni-Se, Ni displayed the energy levels of Ni $2p_{3/2}$, Ni $2p_{1/2}$, and satellite peaks. Also, the main peak of Se 3d existed at 55, with the Se oxide peak at 58.7 eV because of oxidized Se atoms on the sample surface (Fig. S2†).

After material construction, their electrocatalytic performance towards the catalytic HER was studied. All electrochemical measurements were performed in an aqueous medium of potassium hydroxide (KOH; 0.1 M) with the materials initially evaluated through LSV (Fig. 5a). The measured potentials were corrected to eliminate the effect of solution resistance (R_s). This step was done by measuring the open circuit potential (OCP) of each electrode and applying the EIS test at OCP to determine the solution resistance. Then, the potential was processed through the following equation: $E_{final} = E_{measured} - iR_s \times 90\%$. The Ni-S and Ni-P electrodes showed the lowest uncompensated overpotentials at 10 mA cm^{-2}, with readings of 260 and 266 mV, respectively, while after potential loss correction, the overpotential of Ni-S and Ni-P enhanced to be 255 and 263 mV, respectively (Fig. S3a†). The significant effect of removing potential loss appeared at high overpotential values. At 50 mA cm^{-2}, Ni-P gave an overpotential of 394 mV (Fig. 5b) while it gave an overpotential of 358 mV (Fig. S3b†) after resistance compensation with a difference of around 40 mV. The low overpotential observed in the Ni-S electrode may be attributed to the synergistic effect of the NiS and NiS_2 phases, as evidenced by the XRD analysis.[46] Meanwhile, the synergistic effect was further confirmed when the nickel sulfide mixed phases gave better overpotential at 10 mA cm^{-2} (266 mV) than our earlier prepared NiS (single phase), which gave an overpotential of 316 mV.[9] Additionally, the synergistic interaction between $Ni_{12}P_5$, Ni_5P_4, Ni_2P, and NiP_3 phases also had a great influence on efficiency.[50] The expensive Pt/C-40% achieved 38 mV, Ni-Se (305 mV), r-NiO (571 mV), Ni-O- (576 mV), and bare carbon paper (659 mV) at 10 mA cm^{-2} under identical conditions. Notably, the $NiSe_2$ phase gained less attention because of the challenges of its synthesis, although, it has the best electrochemical properties among the other nickel selenide phases.[51] Also, the overpotential of our $NiSe_2$ electrode in this paper is close to the final recorded value of the same phase on the self-supported electrode. This result confirmed the ability of the method to compete with other complex and hard synthetic methods and get close results.[52] At 50 mA cm^{-2}, the order of

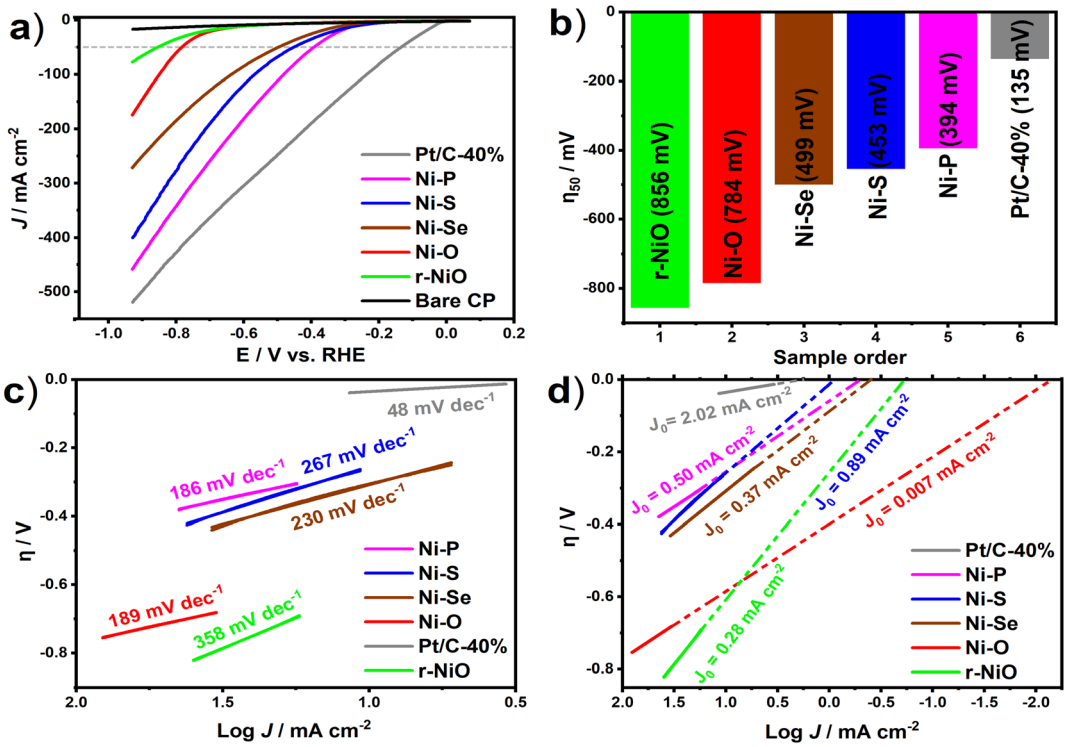

Fig. 5 (a) LSV curves before iR_s-compensation at a scan rate of 10 mV s^{-1}, (b) the overpotential value of each electrode at a current density of 50 mA cm^{-2}, (c) the corresponding Tafel plots of Ni-O, Ni-S, Ni-Se, Ni-P, r-NiO, and Pt/C-40% electrodes, and (d) the estimated exchange currents related to Tafel plots of each electrode.

Table 1 The catalyst performance and their HER kinetic parameters[a]

Catalyst	Overpotential (η)			Tafel slope (b)	Exchange current density (j_0)	Charge transfer coefficient (α)
	η_{10}	η_{50}	η_{100}			
r-NiO	571	856	—	358	0.28	0.16
Ni-O	576	784	851	189	0.007	0.31
Ni-Se	305	499	639	230	0.37	0.26
Ni-S	260	453	571	267	0.89	0.22
Ni-P	266	394	483	186	0.5	0.32

[a] Note: these values are achieved with catalyst loading mass 0.2 mg cm^{-2}.

overpotential values slightly changed to show the superiority of Ni-P (394 mV) to Ni-S (453 mV) and Ni-O (784 mV) to r-NiO (856 mV) (Fig. 5b). The Tafel slopes (b) indicated that the Ni-P catalyst had the most efficient kinetics for hydrogen generation, with a value of 186 mV dec^{-1}, suggesting a shorter reaction pathway. In comparison, the Tafel slope of the Pt/C-40% electrode was 48 mV dec^{-1}. Additionally, the slopes of the remaining electrodes were 189 mV dec^{-1} for Ni-O, 230 mV dec^{-1} for Ni-Se, 267 mV dec^{-1} for Ni-S, and 358 mV dec^{-1} for r-NiO (Fig. 5c). Also, the Tafel slope values were enhanced after applying the resistance correction to be 130 mV dec^{-1} for Ni-P, 156 mV dec^{-1} for Ni-O, 197 mV dec^{-1} for Ni-Se, 225 mV dec^{-1} for Ni-S, and 291 mV dec^{-1} for r-NiO (Fig. S3c†). Generally, all Tafel slopes are larger than 120 mV dec^{-1} which indicates that the water splitting step is the RDS of the reaction which meant the Volmer step controlled the reaction speed.[53,54] Exchange current density (j_0) was the parameter that provided feedback about the kinetics of the overall electrochemical reaction. This term was defined as the rate constant analog for redox reactions, and its value is the anti-log of the Tafel plot line intercept with the X-axis at the equilibrium potential ($\eta = 0$).[55] The Ni-S, Ni-P, Ni-Se, and Ni-O achieved 0.89 mA cm^{-2}, 0.5 mA cm^{-2}, 0.37 mA cm^{-2}, and 0.007 mA cm^{-2} (Fig. 5d). The charge transfer coefficient (α) was another kinetic parameter that referred to the electron jumping efficiency through the electrode–electrolyte interface. This parameter could be computed through the formula, $\alpha = (2.303RT)/(bnF)$ where R is the gas constant, T is the room temperature in kelvin, b is the Tafel slope of each catalyst in volt, n is the number of electrons in the RDS, and F is the Faraday constant.[56] Kinetic parameters of all the catalysts are given in Table 1.

Cyclic voltammetry (CV) was conducted to measure the ECSA, with scan rates of 10, 20, 40, 80, 100, and 150 mV s^{-1} used within a potential window ranging from 0.1 to 0.2 V *versus* a mercury-mercuric oxide (Hg/HgO) reference electrode. The estimated ECSA values were 33.3 cm^2 for Ni-P, 20.7 cm^2 for NiS, and 17.6 cm^2 for Ni-Se, revealing their outstanding performance (Fig. S4†).

To ascertain the charge-transfer resistance (R_{ct}), the electrochemical impedance spectroscopy (EIS) test was conducted at a voltage of −0.53 V *vs.* RHE. The Ni-P electrode revealed the tiniest Nyquist arc, the lowest resistance, and the most rapid transfer of charges, which confirm its catalytic superiority among the other catalysts (Fig. 6a). The lowest resistance of the Ni-P composite could be explained by the large amount of conductive cubic Ni metal and multiple active sites in Ni-P. Following the EIS test, a chronopotentiometry test was conducted to evaluate the durability of the catalysts at a constant current density (100 mA) for 24 hours. Operating a test at a high current value for one day was a step to measure the catalysts performance under industrial-scale simulated conditions in contrast to the previous studies of these compounds at 10 mA cm^{-2}.[47,57,58] Starting with Pt/C-40%, the deterioration in overpotential was about 44%. However, the deterioration percentages of Ni-S and Ni-P were only 6.5% and 11.6%, respectively, after 24 hours of continuous HER performance. Additionally, the Ni-Se electrode almost kept its overpotential stable during the 24 hours while the Ni-O overpotential declined and improved by about 9% (Fig. 6b). The small presence of Ni^0 sites due to reduction occurring on the surface promoted the recombination of H atoms and the material conductivity. It improved the HER rate besides the presence of NiO sites, where H_2O molecules dissociate.[35] After conducting chronopotentiometry measurements for 24 hours, we performed LSV again for all electrodes. It was found that the whole electrode overpotentials at 50 mA cm^{-2} are enhanced or slightly increased except for the benchmark Pt/C (40%) and Ni-Se, both suffered from strong deterioration (Fig. 6c and d).

Then, we ran the long-term chronopotentiometry test on Ni-P for an additional four days. Surprisingly, after replacing the electrolyte solution with a clean one and repeating the test for an extra 24 hours, the electrode showed a stable performance (Fig. 7). This result, combined with the LSV, EIS, and ECSA, revealed the potential of our materials toward the alkaline HER catalytic performance. For further verification, the amount of H_2 gas evolved was analyzed *via* an online GC-TCD system for 5 continuous hours under the same conditions of the chronopotentiometry test in a sealed electrocatalytic cell. The time course of H_2 evolution was recorded as indicated in Fig. S5.† The hydrogen generation rate (HGR) calculated for the Ni-P sample was 2.6 mmol h^{-1} cm^{-2}.[43]

4. Surface process interpretation (HER mechanism)

The reaction on the surface of the efficient catalyst (Ni-P and Ni-S) can be interpreted in detail as the following. Initially, the reaction of water splitting in an alkaline medium starts with

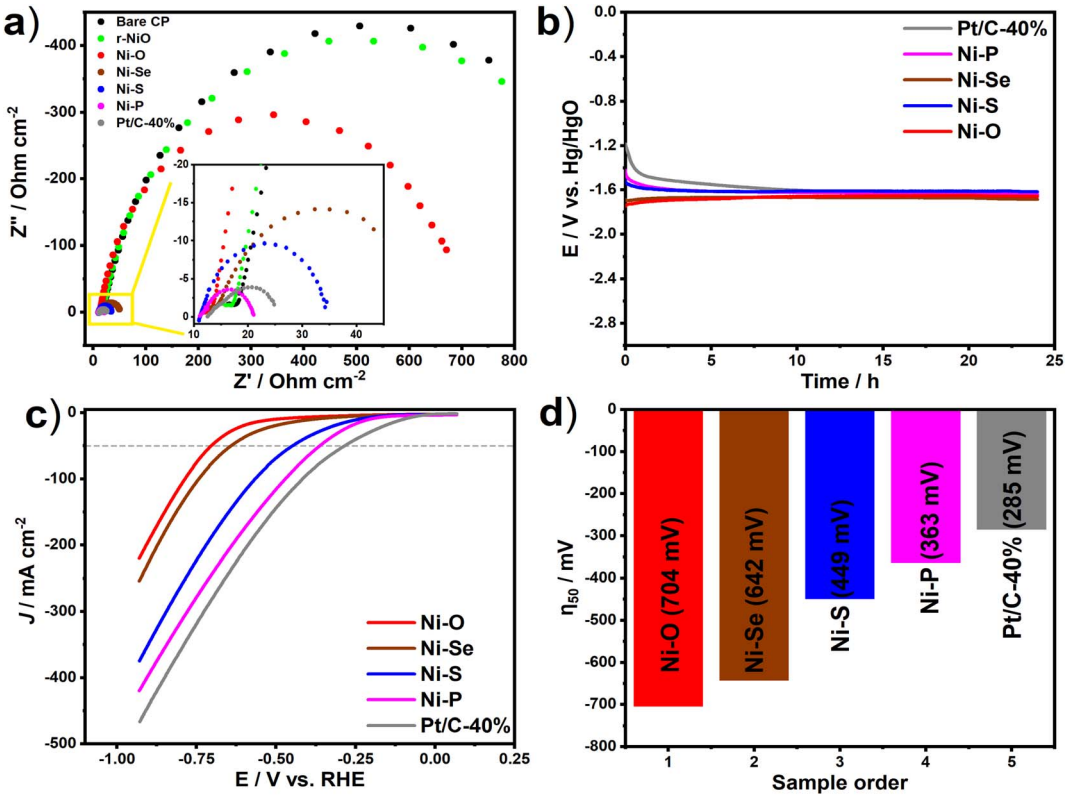

Fig. 6 (a) EIS Nyquist plots of the different electrodes, (b) chronopotentiometry responses of Ni-O, Ni-S, Ni-Se, Ni-P, and Pt/C-40% electrodes at the applied current (100 mA) for 24 h in KOH solution (0.1 M), (c) LSV of Ni-O, Ni-S, Ni-Se, Ni-P, and Pt/C-40% after 24 chronopotentiometry, and (d) the overpotential value of each electrode after chronopotentiometry at a current density of 50 mA cm^{-2}.

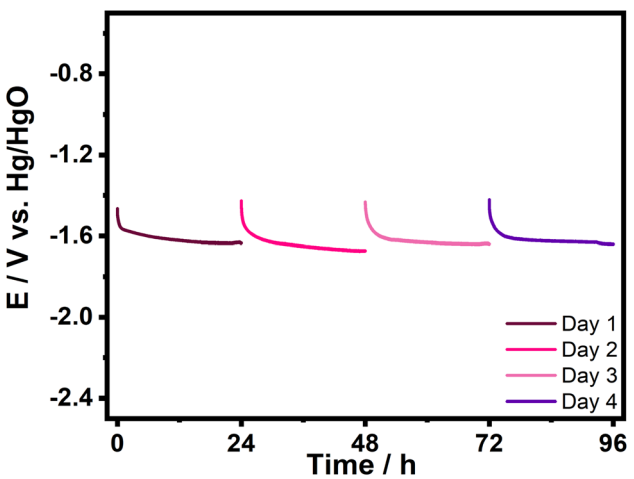

Fig. 7 The chronopotentiometry tests were conducted on four separate days. The measurements taken on the first, third, and fourth days were conducted using a clear solution, while the measurements taken on the second day were conducted in the turbid solution.

water molecule adsorption to form the reactive adsorbed H* atom (Volmer step). One of the two general pathways may follow the Volmer stage: Heyrovsky and Tafel. In the Heyrovsky step, the adsorbed H* atom interacts with another water molecule in the presence of an electron to form an H_2 molecule and OH^- species, which is expected here and is in accordance with our previous studies and DFT calculations.[59] In the Tafel step, two adsorbed H* atoms combine to form an H_2 molecule. Usually, for transition metal compounds the critical stage of the H_2 formation reaction is Volmer (defined by how easily the adsorption and dissociation of H_2O molecules occur). Hence, if we start with the Ni-P surface, the surface consists of two major types of catalytic active species: the high percentage of face-centered cubic Ni^0 atoms and different nickel phosphide phases. The phosphorous atom has a higher electronegativity than the Ni atom, which causes the formation of a partial positive charge on the nickel atom ($Ni^{\delta+}$–$P^{\delta-}$). The negative charge on P generally works as a positively charged proton trapper. In addition, the partial positive charge on Ni weakens the strength of H adsorption and facilitates desorption and H_2 formation. However, the reactivity of the Ni-P catalyst decreases because of the presence of Ni^0 atoms with nickel phosphide phases. Although metallic nickel helps raise the conductivity, it is much more reactive to interact in the HER reaction. The Ni^0 adsorption affinity towards H* is strong, which causes poisoning and blocking of nickel active centers with time. The predominance of metallic nickel may be the main reason beyond the low catalytic activity of the as-prepared Ni-P catalyst compared with nickel phosphides in the literature. In conclusion, the superiority of Ni-P (Ni/Ni_xP_y) may be related to two reasons: (i) the existence of H-acceptor and proton-acceptor active sites in Ni-P,

which improve its catalytic activity and (ii) a high percentage of Ni metal that boosts the catalyst conductivity due to its intrinsic behavior but at the same time, it might promote sensitivity towards poisoning.[9,60,61]

Ni-P and Ni-S have exactly the same working mechanism in enhancing the HER. Both have Ni positively charged atoms because phosphorous and sulfur have higher electronegativity than nickel. Nevertheless, the positive partial charge of nickel in the case of Ni-P is higher than that in Ni-S, as is evident from XPS data. The shifting of the Ni $2p_{3/2}$ peak of Ni-P towards a more elevated positive value (855.9 eV) is greater than that in the case of the Ni $2p_{3/2}$ peak of Ni-S (855.5 eV). This shifting is calculated compared with the same peak value of standard metallic nickel (852.2 eV).[62] Therefore, the catalytic activity of Ni-P towards the HER has appeared to be better than that of Ni-S catalysts.

5. Conclusion

The research has focused on fabricating four Ni-based compounds by calcinating 2D Ni-CP with element sources under various thermal conditions. These synthesized compounds have exhibited high exposed surface area and good electrocatalytic properties. The catalytic activity of these nickel compounds towards the HER was examined through general electrochemical tests, *e.g.*, LSV, EIS, CP, and CV. Among them, Ni-P has shown the lowest Tafel slope and resistance value; moreover, it has exhibited high persistence against activity loss in the HER chronopotentiometry test even when the reaction lasted 96 hours. Also, all prepared compounds have displayed excellent durability compared with commercial Pt/C-40% catalysts in chronopotentiometry. Eventually, the preparation method will be modified to synthesize many transition-metal-based composites and electrocatalyst with nanoparticle morphology to enhance the overall water-splitting reaction.

Conflicts of interest

There is no conflict of interest.

Acknowledgements

M. E. El-Khouly acknowledges the financial support provided from the Egyptian Academy of Scientific Research and Technology through NSFC-ASRT Grant. M. B. Z. acknowledges the financial support received from Alexander von Humboldt Foundation, Grant number Ref 3.4–1211515-EGY-HFST-P.

References

1 M. B. Zakaria, Y. Guo, J. Na, R. Tahawy, T. Chikyow, W. W. El-Said, D. A. El-Hady, W. Alshitari, Y. Yamauchi and J. Lin, Layer-by-Layer Motif Heteroarchitecturing of N,S-Codoped Reduced Graphene Oxide-Wrapped Ni/NiS Nanoparticles for the Electrochemical Oxidation of Water, *ChemSucChem*, 2020, **13**, 3269–3276.

2 J. Noguera-Gómez, M. García-Tecedor, J. Francisco Sánchez-Royo, M. V. Liñán, M. de la Mata, M. Herrera-Collado, S. I. Molina, R. Abargues and S. Giménez, Solution-Processed Ni-Based Nanocomposite Electrocatalysts: An Approach to Highly Efficient Electrochemical Water Splitting, *ACS Appl. Energy Mater.*, 2021, **4**, 5255–5264.

3 Z. Chen, X. Duan, W. Wei, S. Wang and B. J. Ni, Recent advances in transition metal-based electrocatalysts for alkaline hydrogen evolution, *J. Mater. Chem. A*, 2019, **7**, 14971–15005.

4 B. D. Ghasem, A. Mahmood and S. R. Alireza, Nickel nanocones as efficient and stable catalyst for electrochemical hydrogen evolution reaction, *Int. J. Hydrogen Energy*, 2017, **42**, 14560–14565.

5 M. E. El-Khouly, E. El-Mohsnawy and S. Fukuzumi, Solar energy conversion: from natural to artificial photosynthesis, *J. Photochem. Photobiol., C*, 2017, **31**, 36–83.

6 R. Sharma, A. Sharma, S. Agarwal and M. S. Dhaka, Stability and efficiency issues, solutions and advancements in perovskite solar cells: A review, *Sol. Energy*, 2022, **244**, 516–535.

7 F. Ryan, *Triple-Junction III-V Solar Cells with 39.5% AM1.5G and 34.2% AM0 Efficiencies*, United States. 2022, **https://www.osti.gov/servlets/purl/1877360**.

8 D. Maradin, Advantages and disadvantages of renewable energy sources utilization, International Journal of Energy Economics and Policy, *Int. J. Energy Econ. Policy*, 2021, **11**, 176–183.

9 M. B. Z. Hegazy, M. R. Berber, Y. Yamauchi, A. Pakdel, R. Cao and U. P. Apfel, Synergistic Electrocatalytic Hydrogen Evolution in Ni/NiS Nanoparticles Wrapped in Multi-Heteroatom-Doped Reduced Graphene Oxide Nanosheets, *ACS Appl. Mater. Interfaces*, 2021, **13**, 34043–34052.

10 M. B. Zakaria, D. Zheng, U. P. Apfel, T. Nagata, E. S. Kenawy and J. Lin, Dual-Heteroatom-Doped Reduced Graphene Oxide Sheets Conjoined CoNi-Based Carbide and Sulfide Nanoparticles for Efficient Oxygen Evolution Reaction, *ACS Appl. Mater. Interfaces*, 2020, **12**, 40186–40193.

11 L. Wei, G. Lihong, L. Huaming, D. Yilin, X. Bin, O. Bo and K. Erjun, In situ Raman spectroscopic study towards the growth and excellent HER catalysis of Ni/$Ni(OH)_2$ heterostructure, *Int. J. Hydrogen Energy*, 2021, **46**, 26861–26872.

12 E. Ali, Electrocatalysts for hydrogen evolution reaction, *Int. J. Hydrogen Energy*, 2017, **42**, 11053–11077.

13 H. Jin, X. Liu, S. Chen, A. Vasileff, L. Li, Y. Jiao, L. Song, Y. Zheng and S. Z. Qiao, Heteroatom-Doped Transition Metal Electrocatalysts for Hydrogen Evolution Reaction, *ACS Energy Lett.*, 2019, **4**, 805–810.

14 Z. Rubab, P. Erum, Y. Minghui, R. Osama, S. Zubia, A. Maryum and F. Sarah, A review on nickel cobalt sulphide and their hybrids: Earth abundant, pH stable electro-catalyst for hydrogen evolution reaction, *Int. J. Hydrogen Energy*, 2020, **45**, 24518–24543.

15 H. Sun, Z. Yan, F. Liu, W. Xu, F. Cheng and J. Chen, Self-Supported Transition-Metal-Based Electrocatalysts for

Hydrogen and Oxygen Evolution, *Adv. Mater.*, 2019, **32**, 1806326.

16 M. Simon, V. N. Aleksey, M. P. Irina, K. Klaus, C. Erik, O. J. Jens and J. B. Niels, Transition metal carbides (WC, Mo2C, TaC, NbC) as potential electrocatalysts for the hydrogen evolution reaction (HER) at medium temperatures, *Int. J. Hydrogen Energy*, 2015, **40**, 2905–2911.

17 B. A. Yusuf, M. Xie, W. Yaseen, J. Xie and Y. Xu, Hierarchical Ultrathin Defect-rich $CoFe_2O_4$@BC Nanoflowers Synthesized via A temperature-regulated Strategy with Outstanding Hydrogen Evolution Reaction Activity, *Inorg. Chem. Front.*, 2021, **8**, 1455–1467.

18 Y. Zhong, X. Xia, F. Shi, J. Zhan, J. Tu and H. J. Fan, Transition Metal Carbides and Nitrides in Energy Storage and Conversion, *Adv. Sci.*, 2016, **3**, 1500286.

19 L. Wenna, X. Tianyi, Y. Yumin, W. Hong, F. Zhi, D. Zhentao and H. Xinmei, Self-supported Ni3N nanoarray as an efficient nonnoble-metal catalyst for alkaline hydrogen evolution reaction, *Int. J. Hydrogen Energy*, 2021, **46**, 27037–27043.

20 Y. Guo, T. Park, J. W. Yi, J. Henzie, J. Kim, Z. Wang, B. Jiang, Y. Bando, Y. Sugahara, J. Tang and Y. Yamauchi, Nano architectonics for Transition-Metal-Sulfide-Based Electro catalysts for Water Splitting, *Adv. Mater.*, 2019, **31**, 1807134.

21 W. Feng, W. Pang, Y. Xu, A. Guo, X. Gao, X. Qiu and W. Chen, Transition Metal Selenides for Electrocatalytic Hydrogen Evolution Reaction, *ChemElectroChem*, 2020, **7**, 31–54.

22 A. Li, Y. Sun, T. Yao and H. Han, Earth-Abundant Transition-Metal Based Electrocatalysts for Water Electrolysis to Produce Renewable Hydrogen, *Chem.–Eur. J.*, 2018, **24**, 18334–18355.

23 S. Fariba, G. Edward and H. Georges, Electrocatalysis developments for hydrogen evolution reaction in alkaline solutions: A Review, *Int. J. Hydrogen Energy*, 2015, **40**, 256–274.

24 M. Gong, D. Wang, C. C. Chen, B. J. Hwang and H. Dai, A mini review on nickel-based electrocatalysts for alkaline hydrogen evolution reaction, *Nano Res.*, 2016, **9**, 28–46.

25 P. F. Liu, L. Zhang, L. R. Zheng and H. G. Yang, Surface engineering of nickel selenide for an enhanced intrinsic overall water splitting ability, *Mater. Chem. Front.*, 2018, **2**, 1725–1731.

26 R. Geva, N. R. Levy, J. Tzadikov, R. Cohen, M. Weitman, L. Xing, L. Abisdris, J. Barrio, J. Xia, M. Volokh, Y. Ein-Eli and M. Shalom, Molten state synthesis of nickel phosphides: mechanism and composition-activity correlation for electrochemical applications, *J. Mater. Chem. A*, 2021, **9**, 27629–27638.

27 C. Qinghe, W. Chuanqin, C. Shujie, X. Xingdong, L. Fenggang, G. Xinhua and W. Jiahai, Vertically aligned NiP_2 nanosheets with interlaced mesh network for highly efficient water splitting under alkaline and acid solutions, *Int. J. Hydrogen Energy*, 2019, **44**, 6535–6543.

28 Y. Yang, X. Sun, G. Han, X. Liu, X. Zhang, Y. Sun, M. Zhang, Z. Cao and Y. Sun, Enhanced Electrocatalytic Hydrogen Oxidation on Ni/NiO/C Derived from a Nickel-Based Metal–Organic Framework, *Angew. Chem., Int. Ed.*, 2019, **58**, 10644–10649.

29 R. T. Zahraa, K. S. Ahmada, C. Zequineb, R. K. Guptab, A. G. Thomas and M. A. Malik, Evaluation of electrochemical properties for water splitting by NiO nanocubes synthesized using Olea ferruginea, *Sustain. Energy Technol. Assess.*, 2020, **40**, 100753.

30 Z. Ge, B. Fu, J. Zhao, X. Li, B. Ma and Y. Chen, A review of the electrocatalysts on hydrogen evolution reaction with an emphasis on Fe, Co and Ni-based phosphides, *J. Mater. Sci.*, 2020, **55**, 14081–14104.

31 N. Jiang, Q. Tang, M. Sheng, B. You, D. Jiang and Y. Sun, Nickel sulfides for electrocatalytic hydrogen evolution under alkaline conditions: a case study of crystalline NiS, NiS_2, and Ni_3S_2 nanoparticles, *Catal. Sci. Technol.*, 2016, **6**, 1077–1084.

32 D. Jieting, J. Shan, W. Hui, G. Hengjun, L. Fusheng, L. Vladimir and W. Rongfang, Mesoporous nickel-sulfide/nickel/N-doped carbon as HER and OER bifunctional electrocatalyst for water electrolysis, *Int. J. Hydrogen Energy*, 2019, **44**, 2832–2840.

33 Z. Zou, X. Wang, J. Huang, Z. Wu and F. Gao, An Fe-doped nickel selenide nanorod/nanosheet hierarchical array for efficient overall water splitting, *J. Mater. Chem. A*, 2019, **7**, 2233–2241.

34 C. Wang, Y. Li, X. Wang and J. Tu, N-Doped NiO Nanosheet Arrays as Efficient Electrocatalysts for Hydrogen Evolution Reaction, *J. Electron. Mater.*, 2021, **50**, 5072–5080.

35 A. Y. Faid, A. O. Barnett, F. Seland and S. Sunde, Ni/NiO nanosheets for alkaline hydrogen evolution reaction: In situ electrochemical Raman study, *Electrochim. Acta*, 2020, **361**, 137040.

36 N. Asim, S. Ahmadi, M. A. Alghoul, F. Y. Hammadi, K. Saeedfar and K. Sopian, Research and Development Aspects on Chemical Preparation Techniques of Photoanodes for Dye Sensitized Solar Cells, *Int. J. Photoenergy*, 2014, **2014**, 518156.

37 M. Hu, S. Ishihara and Y. Yamauchi, Bottom-Up Synthesis of Monodispersed Single-Crystalline Cyano-Bridged Coordination Polymer Nanoflakes, *Angew. Chem., Int. Ed.*, 2013, **52**, 1235–1239.

38 M. B. Zakaria, M. Hu, R. P. Salunkhe, M. Pramanik, K. Takai, V. Malgras, S. Choi, S. X. Dou, J. H. Kim, M. Imura, S. Ishihara and Y. Yamauchi, Controlled Synthesis of Nanoporous Nickel Oxide with Two-Dimensional Shapes through Thermal Decomposition of Metal– Cyanide Hybrid Coordination Polymers, *Chemistry*, 2015, **21**, 3605–3612.

39 W. C. Fernelius, *Inorganic Syntheses*, vol. 2, 1946.

40 M. M. K. Motlagh, A. A. Youzbashi and L. Sabaghzadeh, Synthesis and characterization of Nickel hydroxide/oxide nanoparticles by the complexation-precipitation method, *Int. J. Phys. Sci.*, 2011, **6**, 1471–1476.

41 H. Fan, H. Yu, X. L. Wu, Y. Zhang, Z. Z. Luo, H. Wang, Y. Guo, S. Madhavi and Q. Yan, Controllable Preparation of Square Nickel Chalcogenide (NiS and $NiSe_2$) Nanoplates for Superior Li/Na ion Storage Properties, *ACS Appl. Mater. Interfaces*, 2016, **8**, 25261–25267.

42 M. B. Zakaria, C. Li, M. Pramanik, Y. Tsujimoto, M. Hu, V. Malgras, S. Tominaka and Y. Yamauchi, Nanoporous Mn-based electrocatalysts through thermal conversion of cyano-bridged coordination polymers toward ultra-high efficiency hydrogen peroxide production, *J. Mater. Chem. A*, 2016, **4**, 9266–9274.

43 M. B. Zakaria, K. Harrath, D. Tetzlaff, M. Smialkowski, D. Siegmund, J. Li and R. Cao, Apfel UP. Boosting the overall electrochemical water splitting performance of pentlandites through non-metallic heteroatom incorporation, *iScience*, 2022, **25**, 105148.

44 J. Silvia-Avalos, M. G. Richmond, T. Nagappan and D. A. Kunz, Degradation of the Metal-Cyano Complex Tetracyanonickelate(II) by Cyanide-Utilizing Bacterial Isolates, *Appl. Environ. Microbiol.*, 1990, 3664–3670.

45 R. Jin-Tao and Y. Zhong-Yong, Hierarchical nickel sulfide nanosheets directly grown on Ni foam: a stable and efficient electrocatalyst for water reduction and oxidation in alkaline medium, *ACS Sustainable Chem. Eng.*, 2017, **5**, 7203–7210.

46 Q. Li, D. Wang, C. Han, X. Ma, Q. Lu, Z. Xing and X. Yang, Construction of amorphous interface in an interwoven NiS/NiS_2 structure for enhanced overall water splitting, *J. Mater. Chem. A*, 2018, **6**, 8233–8237.

47 X. Wu, B. Yang, Z. Li, L. Lei and X. Zhang, Synthesis of supported vertical NiS_2 nanosheets for hydrogen evolution reaction in acidic and alkaline solution, *RSC Adv.*, 2015, **5**, 32976–32982.

48 P. Yuan, L. Yanru, Z. Jinchong, Y. Kang, L. Jilei, L. Dandan, W. Hu, D. Liu, Y. Liu and C. Liu, Monodispersed nickel phosphide nanocrystals with different phases: synthesis, characterization and electrocatalytic properties for hydrogen evolution, *J. Mater. Chem. A*, 2015, **3**, 1656–1665.

49 D. Basundhara, N. H. Jan, B. Rodrigo, K. Shweta, L. Konstantin, Z. Ingo, M. Driess and P. W. Menezes, A Facile Molecular Approach to Amorphous Nickel Pnictides and Their Reconstruction to Crystalline Potassium-Intercalated γ-NiOOHx Enabling High-Performance Electrocatalytic Water Oxidation and Selective Oxidation of 5-Hydroxymethylfurfural, *Small*, 2023, 2301258.

50 C. Hu, J. Cai, S. I. Liu, C. Lv, J. Luo, M. Duan, C. Chen, Y. Shi, J. Song, Z. Zhang, A. Watanabe, E. Aoyagi and S. Ito, A General Strategy for Preparation of Porous Nickel Phosphide Nanosheets on Arbitrary Substrates toward Efficient Hydrogen Generation, *ACS Appl. Energy Mater.*, 2020, **3**, 1036–1045.

51 S. Anantharaj, S. Kundu and S. Noda, Progress in nickel chalcogenide electrocatalyzed hydrogen evolution reaction, *J. Mater. Chem. A*, 2020, **8**, 4174–4192.

52 Y. Sun, K. Z. KZ, H. Li, T. Zhang, X. Li, W. Cai, J. Ma, H. J. Fan and Y. Li, Strong Electronic Interaction in Dual-Cation-Incorporated $NiSe_2$ Nanosheets with Lattice Distortion for Highly Efficient Overall Water Splitting, *Adv. Mater.*, 2018, **30**, 1802121.

53 S. Anantharaj, S. Noda, V. R. Jothi, S. C. Yi, M. Driess and P. W. Menezes, Strategies and Perspectives to Catch the Missing Pieces in Energy-Efficient Hydrogen Evolution Reaction in Alkaline Media, *Angew. Chem., Int. Ed.*, 2021, **60**, 18981–19006.

54 L. Andrzei, Mechanism and kinetics of the hydrogen evolution reaction, *Int. J. Hydrogen Energy*, 2019, **44**, 19484–19518.

55 F. Barbir, Fuel Cell Electrochemistry, in *PEM Fuel Cells Theory and Practice*, Academic Press, 2005, ch. 3, pp. 33–72.

56 A. F. Alharbi, A. A. M. Abahussain, W. Wazeer, H. El-Deeb and A. B. Ahmed Amine Nassr, Stainless steel as gas evolving electrodes in water electrolysis: Enhancing the activity for hydrogen evolution reaction via electrodeposition of Co and CoP catalysts, *Int. J. Hydrogen Energy*, 2023, **48**, 31172–31186.

57 Y. Ge, S. Gao, P. Dong, R. Baines, P. M. Ajayan, M. Ye and J. Shen, Insight into the hydrogen evolution reaction of nickel dichalcogenide nanosheets: activities related to non-metal ligands, *Nanoscale*, 2017, **9**, 5538–5544.

58 W. Kim, D. K. Cho, H. W. Lim, K. Kim, S. Hong and J. Y. Kim, Phase-dependent hydrogen evolution activity of nickel phosphide nanosheet arrays in alkaline electrolytes, *Electrochim. Acta*, 2020, **344**, 136116.

59 M. B. Zakaria, L. Bahri, D. Tetzlaff, S. A. Sandena and U. Apfel, Silicon atom doping in heterotrimetallic sulfides for non-noble metal alkaline water electrolysis, *Energy Adv.*, 2023, **2**, 1190–1203.

60 C. Y. Lin, S. C. Huang, Y. G. Lin, L. C. Hsu and C. T. Yi, Electro synthesized Ni-P nanospheres with high activity and selectivity towards photoelectrochemical plastics reforming, *Appl. Catal., B*, 2021, **296**, 120351.

61 L. K. Putri, B. Ng, R. Y. Zhong Yeo, W. Ong, A. R. Mohamed and S. Chai, Engineering nickel phosphides for electrocatalytic hydrogen evolution: A doping perspective, *J. Chem. Eng.*, 2023, **461**, 141845.

62 G. Chen, T. Y. Ma, Z. Liu, N. Li, Y. Su, K. Davey and S. Qiao, Efficient and Stable Bifunctional Electrocatalysts Ni/Ni x M y (M = P, S) for Overall Water Splitting, *Adv. Funct. Mater.*, 2016, **26**, 3314–3323.